OPEN ACCESS
IOP Publishing | International Atomic Energy Agency
Nuclear Fusion
Nucl. Fusion **59** (2019) 112019 (13pp)
https://doi.org/10.1088/1741-4326/ab205e

Overview of recent TJ-II stellarator results

E. Ascasíbar[1], D. Alba[1], D. Alegre[1], A. Alonso[1], J. Alonso[1], F. de Aragón[1], A. Baciero[1], J.M. Barcala[2], E. Blanco[1], J. Botija[1], L. Bueno[1], S. Cabrera[1], E. de la Cal[1], I. Calvo[1], A. Cappa[1], D. Carralero[1], R. Carrasco[1], B. Carreras[3], F. Castejón[1], R. Castro[1], A. de Castro[1], G. Catalán[1], A.A. Chmyga[4], M. Chamorro[1], A.W. Cooper[5], A. Dinklage[6], L. Eliseev[7], T. Estrada[1], M. Ezzat[1], F. Fernández-Marina[1], J.M. Fontdecaba[1], L. García[3], I. García-Cortés[1], R. García-Gómez[1], J.M. García-Regaña[1], A. González-Jerez[1], G. Grenfell[8], J. Guasp[1], J. Hernández-Sánchez[1], J. Hernanz[1], C. Hidalgo[1], E. Hollmann[9], A. Jiménez-Denche[1], P. Khabanov[7], N. Kharchev[10], I. Kirpitchev[1], R. Kleiber[6], A.S. Kozachek[4], L. Krupnik[4], F. Lapayese[1], M. Liniers[1], B. Liu[11], D. López-Bruna[1], A. López-Fraguas[1], B. López-Miranda[1], J. López-Rázola[1], U. Losada[1], E. de la Luna[1], A. Martín de Aguilera[1], F. Martín-Díaz[1], M. Martínez-Fuentes[1], G. Martín-Gómez[1], A.B. Martín-Rojo[1], J. Martínez-Fernández[1], K.J. McCarthy[1], F. Medina[1], M. Medrano[1], L. Melón[1], A.V. Melnikov[7], P. Méndez[1], R. Merino[1], F.J. Miguel[1], B. van Milligen[1], A. Molinero[2], B. Momo[8], P. Monreal[1], S. Mulas[1], Y. Narushima[12], M. Navarro[1], M. Ochando[1], S. Ohshima[13], J. Olivares[1], E. Oyarzábal[1], J.L. de Pablos[1], L. Pacios[1], N. Panadero[1], F. Parra[14], I. Pastor[1], A. de la Peña[1], A. Pereira[1], J.R. Pinzón[15], A.B. Portas[1], E. Poveda[1], J.A. Quintana[1], F.J. Ramos[1], G.A. Rattá[1], M. Redondo[1], E. Rincón[1], L. Ríos[1], C. Rodríguez-Fernández[1], L. Rodríguez-Rodrigo[1], B. Rojo[1], A. Ros[1], E. Rosa[1], E. Sánchez[1], J. Sánchez[1], M. Sánchez[1], E. Sánchez-Sarabia[1], S. Satake[12], J.A. Sebastián[1], R. Sharma[16], C. Silva[16], E.R. Solano[1], A. Soleto[1], B.J. Sun[1], F.L. Tabarés[1], D. Tafalla[1], H. Takahashi[12], N. Tamura[12], A. Tolkachev[1], J. Vega[1], G. Velasco[1], J.L. Velasco[1], S. Yamamoto[13], B. Zurro[1] and the TJ-Team[1]

[1] National Fusion Laboratory, CIEMAT, Madrid, Spain
[2] Department of Technology, CIEMAT, Madrid, Spain
[3] Universidad Carlos III, Madrid, Spain
[4] Institute of Plasma Physics, NSC KIPT Kharkov, Ukraine
[5] Swiss Alps Fusion Energy (SAFE), Vers l'Eglise, Switzerland
[6] Max-Planck-Institut für Plasmaphysik, Greifswald, Germany
[7] National Research Centre 'Kurchatov Institute', Moscow, Russian Federation
[8] Consorzio RFX (CNR, ENEA, INFN, Universitá di Padova, Acciaierie Venete SpA), Padova, Italy
[9] University of California-San Diego, San Diego, CA, United States of America
[10] General Physics Institute, Russian Academy of Sciences, Moscow, Russian Federation
[11] ENN Energy Research Institute, Langfang, Hebei, China
[12] National Institute for Fusion Science, Toki, Japan
[13] Institute of Advanced Energy, Kyoto University, Uji, Japan
[14] Rudolf Peierls Centre for Theoretical Physics, University of Oxford, Oxford, United Kingdom of Great Britain and Northern Ireland
[15] Max-Planck-Institut für Plasmaphysik, Garching, Germany
[16] IPFN, Instituto Superior Técnico, Universidade de Lisboa, Lisboa, Portugal

E-mail: enrique.ascasibar@ciemat.es

Received 23 November 2018, revised 8 April 2019
Accepted for publication 9 May 2019
Published 24 July 2019

Abstract

The main results obtained in the TJ-II stellarator in the last two years are reported. The most important topics investigated have been modelling and validation of impurity transport, validation of gyrokinetic simulations, turbulence characterisation, effect of magnetic configuration on transport, fuelling with pellet injection, fast particles and liquid metal plasma facing components.

As regards impurity transport research, a number of working lines exploring several recently discovered effects have been developed: the effect of tangential drifts on stellarator neoclassical transport, the impurity flux driven by electric fields tangent to magnetic surfaces and attempts of experimental validation with Doppler reflectometry of the variation of the radial electric field on the flux surface. Concerning gyrokinetic simulations, two validation activities have been performed, the comparison with measurements of zonal flow relaxation in pellet-induced fast transients and the comparison with experimental poloidal variation of fluctuations amplitude. The impact of radial electric fields on turbulence spreading in the edge and scrape-off layer has been also experimentally characterized using a 2D Langmuir probe array. Another remarkable piece of work has been the investigation of the radial propagation of small temperature perturbations using transfer entropy. Research on the physics and modelling of plasma core fuelling with pellet and tracer-encapsulated solid-pellet injection has produced also relevant results. Neutral beam injection driven Alfvénic activity and its possible control by electron cyclotron current drive has been examined as well in TJ-II. Finally, recent results on alternative plasma facing components based on liquid metals are also presented.

Keywords: stellarator, impurity transport, gyrokinetic simulations, electric fields, turbulence, Alfvénic activity, liquid metal plasma facing components

(Some figures may appear in colour only in the online journal)

1. Introduction

The TJ-II stellarator (heliac type, major radius 1.5 m, minor radius $\leqslant$0.22 m, four periods, average magnetic field on axis 0.95 T, plasma volume $\leqslant$1 m^3) is entering its third decade of operation. Both electron cyclotron resonance heating (ECRH) (two gyrotrons, 53.2 GHz, P $\leqslant$ 300 kW each, suitable for X2 heating) and neutral beam injection (NBI) heating (two H^0 injectors, E $\leqslant$ 30 kV, P $\leqslant$ 600 kW each) can be used to produce and sustain the discharge. Plasma physics research in TJ-II is focused on some selected areas posing fundamental problems that must be solved in the development of reactor-grade magnetic confinement devices, namely: impurity accumulation in stellarators, turbulence, effects of the magnetic configuration on transport in stellarators, plasma core fuelling with PI, fast particle driven modes, power exhaust physics and technology, among others. The very wide range of configuration flexibility of the device (edge rotational transform can be varied from 1.0 to 2.2) and its rather complete set of advanced diagnostics have been instrumental for the plasma research done so far by the TJ-II team. In recent years, a substantial effort has been put into strengthening the team's modelling capability in order to tackle the validation of theory in the areas of transport, turbulence, magnetic topology, electric fields, fast particles and the relations among them. Whenever feasible the modelling results have been extended to the largest stellarators/heliotrons in operation, namely the Large Helical Device (LHD) and Wendelstein 7-X (W7-X). It must be noted that work done on TJ-II is relevant for both W7-X and the LHD and it also aims to promote synergies between the tokamak and stellarator lines through its contributions to ITER and ITPA research programmes.

This paper reports the main results obtained in the last two years and is organised along the list of topics mentioned in the abstract, each section covering one of them.

2. Neoclassical impurity transport

Impurity accumulation is one of the main problems that limit the plasma performance via increased radiative losses and plasma dilution. For stellarator reactor-relevant conditions, accumulation is explained as due to the negative (inwards pointing) radial electric field required to satisfy the ambipolarity constraint on the neoclassical particle fluxes. But there are some experimental observations of outward impurity flux not well understood in stellarators [1, 2] that call for improvements of the neoclassical theory. In this context a number of working lines exploring several recently discovered effects are being developed.

2.1. Effect of tangential drifts on stellarator neoclassical transport and discussion on the solutions for φ_1 in low collisionality regimes

Two important ingredients have often been neglected in standard neoclassical theory and simulations of stellarator plasmas. First, the component of the electrostatic potential that is non-constant along the flux surface, that we denote by φ_1. Only recently has it been acknowledged [3] that φ_1 can affect radial impurity transport via the radial $E \times B$ advection of the variations of impurity density along the flux surfaces, which has triggered the interest in its calculation [4–8]. The computation of φ_1 has been included in some modern neoclassical codes, but the number of simulations in which φ_1 has been calculated is still scarce [4]. The systematic analytical description of φ_1 has received little consideration as well. The second ingredient that has often been missing in stellarator neoclassical calculations is the component of the magnetic drift that is tangent to the flux surface, whose effect is essential to correctly determine the radial neoclassical fluxes of the bulk ions at low collisionality and small radial electric field values.

In [9], low collisionality neoclassical equations that include φ_1 and the tangential magnetic drift have been rigorously derived for sufficiently optimized stellarators, and the radial neoclassical fluxes for the main ions have been computed in the $1/\nu$, $\sqrt{\nu}$ and superbanana-plateau regimes. Besides, it has been proven that φ_1 can become especially large in plasma regimes in which the tangential magnetic drift counts. Therefore, the two ingredients mentioned above must be simultaneously and consistently treated, in general. The orbit averaged code KNOSOS (KiNetic Orbit-averaging-SOlver for Stellarators), recently developed, has been used to solve the equations derived in [9].

In [10], a thorough analysis of the solutions for φ_1 in the $1/\nu$, $\sqrt{\nu}$ and superbanana-plateau regimes has been presented. The different asymptotic regimes for φ_1 have been identified analytically and verified with KNOSOS.

2.2. Effect of tangential magnetic drifts on the calculation of φ_1 for realistic stellarator plasmas: LHD stellarator

Calvo *et al* [10] used academic configurations and plasma profiles in order to illustrate the different neoclassical regimes. In [5], it has been proven that the tangential magnetic drift is also relevant for the calculation of φ_1 in realistic stellarator plasmas. We have chosen, for the LHD, two different scenarios: medium density [11] and low density with very high ion temperature. The latter presents a specially small negative radial electric field [12], a situation in which the contribution of the superbanana- plateau regime to bulk ion transport is expected to be largest. The numerical calculations were done with the code KNOSOS following [9], and the results for the high-temperature plasma are shown in figure 1. On the left, a calculation in which the tangential magnetic drift is artificially switched off is depicted. On the right, it can be observed that the calculation that keeps the tangential magnetic drift yields a quite larger φ_1, with a different phase. These phase differences are likely to have a strong impact on the impurity transport driven by tangential electric fields, a matter that will be discussed later in the paper. Experiments have been planned for the incoming deuterium campaigns of the LHD [13] in order to validate these predictions. It is worth noting that the calculations were performed with a version of KNOSOS that relied on the splitting of the magnetic field strength into two parts, one corresponding to a perfectly optimized stellarator, and one corresponding to the deviation from it. This splitting cannot be accurately done for the LHD and this may give rise to quantitative inaccuracies (that are discussed in [5]), although the qualitative results are expected to hold.

2.3. Impurity flux driven by electric fields tangent to magnetic surfaces in stellarators

The standard argument to explain the accumulation of impurities with $Z \gg 1$ relies on the, in principle, large inward pinch in the neoclassical radial impurity flux, Γ_z, caused by the typically negative stellarator radial electric field E_r. This argument was proven to be flawed, at least in some important cases, in [14], where it was shown that, if the main ions have low collisionality and the impurities are collisional, then Γ_z does not depend on E_r. This result was interpreted in a positive way because it diminished the prevalence of E_r in Γ_z and made 'temperature screening' (that is, the reduction or absence of impurity accumulation thanks to the contribution of the temperature gradient to Γ_z) more likely than previously thought.

In [14], the effect of φ_1 on Γ_z was not included. In [6], we give an analytical calculation of Γ_z for low collisionality main ions and collisional impurities, incorporating the effect of φ_1. We show that this effect can be very strong for $Z \gg 1$ and that, once it is taken into account, the dependence of Γ_z on E_r reappears. In addition, we prove that such an effect is stellarator specific (i.e. Γ_z in a tokamak does not depend on E_r, whatever φ_1). A careful analysis of the final expression for Γ_z in stellarators (that reduces to the expression derived in [14] when φ_1 vanishes) reveals that the impact of φ_1 starts to be important for $e|\varphi_1|/T = O(\epsilon)$, where ϵ is the inverse aspect ratio. Our analytical results have been applied to the calculation of the neoclassical particle flux Γ_z versus E_r, for three charge states of tungsten in an LHD plasma, see [6]. The computation of φ_1 has been carried out with the code EUTERPE. The results show a large difference in the neoclassical impurity flux obtained with and without φ_1, and a strong dependence of the flux on E_r when φ_1 is included. Although the effect of φ_1 is typically to increase impurity accumulation, there is a small region in parameter space where its inclusion leads to impurity expulsion.

2.4. Experimental validation with Doppler reflectometry of the variation of the radial electric field on the flux surface in electron-root stellarator plasmas

The interest in the role of the electric field tangent to the surface on the transport of impurities, commented in section 2.1,

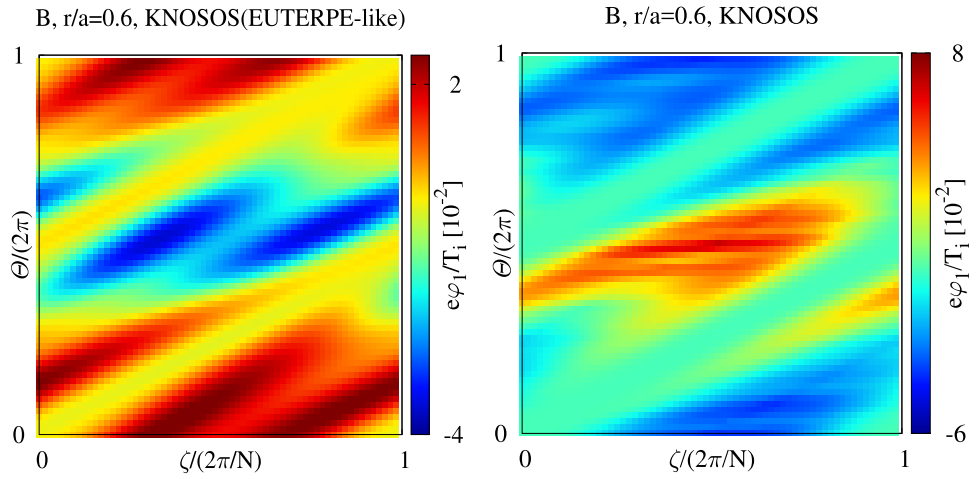

Figure 1. Calculations of φ_1 with the KNOSOS code, at normalised radius, $r/a = 0.6$. Left: with the tangential magnetic drift artificially switched off. Right: keeping the tangential magnetic drift. Note the different scales in both plots. Reproduced from [5]. © 2018 Laboratorio Nacional de Fusion, CIEMAT.

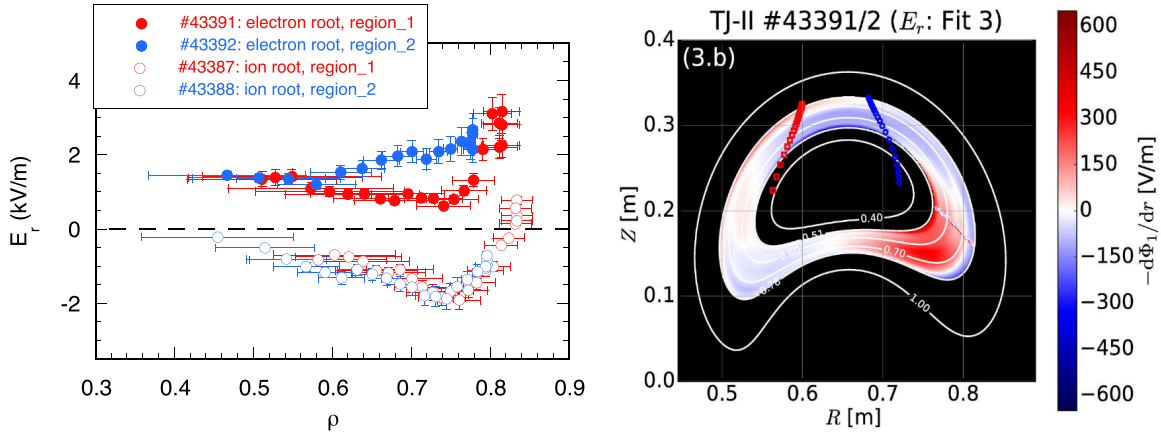

Figure 2. Left: E_r profiles measured by the Dopppler reflectometer at turbulence scales $k_\perp \sim 6$–$8\,\mathrm{cm}^{-1}$, in the two plasma regions (1 in red and 2 in blue) in both electron and ion root regimes. Right: calculated contribution to the radial electric field component that arises from the radial dependency of φ_1. Reproduced from [7]. © 2018 CIEMAT. Plasma regions 1 and 2 are indicated by consistently coloured thick lines in the upper (external) part of the plasma cross section.

has dealt in most cases with ion-root plasmas, whereas electron root conditions have been barely investigated. On the other hand, since φ_1, the part of the electrostatic potential that leads to the electric field tangent to the surface, depends parametrically on the flux surface label as well, it can cause variations of the total radial electric field over the flux surface.

These two elements of the problem have been recently addressed [7] motivated by the observation of strong differences in the total radial electric field measured at different points over the same flux surface with the TJ-II Doppler reflectometer (DR) in electron-root plasmas (see figure 2, left). In figure 2, right, we show the calculated contribution to the radial electric field component that arises from the radial dependency of φ_1 for a TJ-II electron-root plasma (shots 43391 and 43392). Although the agreement at the specific DR measurement positions has not been quantitatively captured by the numerical simulations performed with the EUTERPE code (see [7] for details), the fact that those differences occur in electron-root conditions and are practically absent under ion-root has been well reproduced by the simulations. Similar results were obtained closer to the plasma edge in [15]. Moreover, the simulation and experimental analysis of asymmetric radiation patterns resulting from φ_1-driven inhomogeneous impurity density in TJ-II, in electron- and ion-root plasmas, are ongoing.

Motivated by the fact of having similar DR systems installed in W7-X, a plasma presenting core electron root confinement (CERC) conditions, produced in the first W7-X campaign [16–18], has been also considered for carrying out a similar analysis.In particular a high mirror configuration has been chosen due to its higher ripple in comparison with the standard configuration used in our previous work [4] and due to its higher likeliness to exhibit large φ_1 values and related effects. The results obtained, see figure 3, show that the region of the core in electron-root (inside $r/a = 0.6$ approximately) shows considerably larger φ_1 amplitude than the region in ion root, which can lead to large radial electric field differences over flux surfaces in the vicinity of the root transition. The substantially different results obtained with adiabatic or kinetic electrons confirms the need of making use of the latter for an

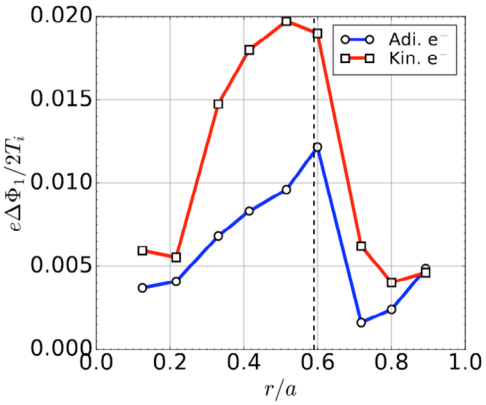

Figure 3. EUTERPE calculation with both kinetic (red) and adiabatic (blue) electrons of the maximum difference of φ_1, normalized to the ion temperature, over several flux surfaces of a high ripple W7-X configuration in CERC plasma conditions. The dashed vertical line indicates the radial position where $E_r = 0$. On the left and right of this line the input radial electric field is positive and negative, respectively. Reproduced from [7]. © 2018 CIEMAT.

accurate calculation of φ_1, which, as shown in other works [8], can be larger than previously estimated in W7-X [4].

3. Experimental validation of global gyrokinetic simulations

Zonal flows (ZF) are recognized as an important mechanism for the self regulation of plasma turbulence. The appropriate framework to study plasma turbulence is the gyrokinetic formalism, in which kinetic simulations are affordable using appropriate codes and supercomputers. However, these codes should be carefully validated against experiment in order to be reliable. Scale resolved turbulence measurements are important to validate the simulations and to identify the type of turbulence at work. Some properties of ZFs and plasma turbulence have been simulated and experimentally validated in TJ-II.

3.1. Comparison between measurements of zonal flow relaxation in pellet-induced fast transients and gyrokinetic simulations

The linear ZF relaxation in stellarator geometries has been studied from different perspectives. The problem of linear collisionless relaxation of ZFs in TJ-II was first studied in numerical simulations in [19]. From the analytical point of view, the long-term collisionless relaxation of zonal potential perturbations has been studied in [20–23]. In particular, it has been proven that the relaxation process in stellarators exhibits a characteristic low frequency oscillation (that is absent in tokamaks), and analytical approximations for this frequency have been derived. In [23] semianalytical predictions were compared to results of numerical simulations carried out with the gyrokinetic codes GENE [24] and EUTERPE [25] in different stellarators (TJ-II, W7-X and the LHD). Good agreement has been found between analytical estimations of the ZF oscillation frequency and the results from numerical simulations.

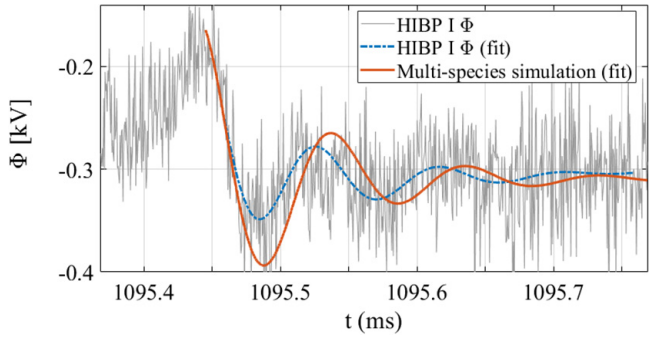

Figure 4. Comparison of a potential relaxation experimentally measured by the HIBP diagnostic in plasma discharge 39063, the corresponding fit (in blue) and the fit of multi-ion simulated relaxation (in orange) to a damped oscillatory model (including the correction to the frequency introduced by formula 21 from [29]). Reproduced from [28]. CC BY 4.0.

This cross-benchmark has allowed not only testing the analytical calculations but also verifying the codes in this setting.

During pellet injection (PI) experiments in TJ-II [26, 27], a sudden global perturbation to the plasma potential was detected at the radial location of pellet ablation which undergoes a fast oscillatory relaxation, see figure 4. This phenomenon was studied numerically in global linear gyrokinetic simulations with the code EUTERPE, using the experimental plasma profiles as input for the simulations [28]. This constituted the first experimental observation of the LFO predicted analytically in [21]. The numerical simulations of oscillation frequency and damping rate of the potential oscillations reproduced qualitatively the experimental oscillations, although a quantitative agreement was not found in the first single-species simulations.

In a second step, the ZF relaxation has been studied numerically in a multi-species plasma with TJ-II configurations [29]. Multi-species collisional simulations carried out with the experimental plasma profiles from the PI experiments previously analyzed in [28] showed an improved quantitative agreement in frequency and damping rate between experiment and simulations [29], as shown in figure 5. The damping rate is significantly increased when impurities are considered in the simulation. Simulations including impurities and adiabatic electrons showed a reduced oscillation frequency with respect to the single-ion case but the extrapolation for a multi-species plasma with kinetic-electrons, using formula 21 from [29], gives frequency values closer to the experimental ones. Figure 5 shows the overall agreement between ensembles of experimental and simulated data obtained using the above mentioned multi-ion adiabatic-electron simulations and the extrapolation using formula 21 from [29]. The agreement between ensembles is better than the one for individual shots due to experimental uncertainties.

It must be noted that in the present state of the EUTERPE code the gyro-kinetic version employed in this section does not include any term related to the electrostatic potential variation provided as output by the neoclassical version. The inclusion of those terms into the gyro-kinetic version (e.g. considering the modified neoclassical equilibrium as background distribution, or including the related $E \times B$ drift and mirror terms)

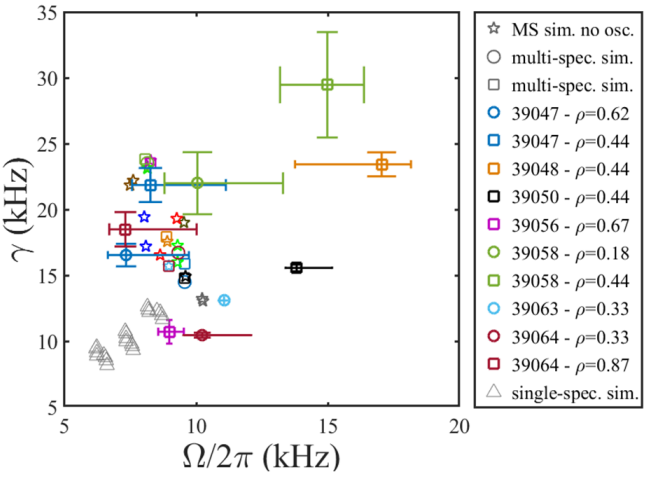

Figure 5. Damping rate (γ) versus oscillation frequency (Ω) for the experimental oscillations detected in [28]. Data are shown for the specified TJ-II discharges and for numerical simulations, both with a single (grey triangles) and with multiple kinetic species, namely hydrogen ions + electrons + C^{4+} impurity ions (circles, squares and pentagrams) [29].The same color is used for experimental points (showing error bars) and for multi-species simulated discharges (without error bars). Note that some plotted discharges showed no oscillations (pentagrams). For some discharges with insufficient profile data, profiles from a similar discharge were used in the simulation. In the first three rows of the legend, symbols are shown with a single grey color to avoid an excessive legend length. The multi-species simulation data in this figure are corrected relative to a previous version in figure 13 from [29].

may be important when impurities are taken into account, and their absence so far may be a source of disagreement between experiment and simulation. The first steps towards the coupling of both versions are currently being made.

3.2. Validation of gyrokinetic simulations with density fluctuations spectra measured by Doppler reflectometry

Global gyrokinetic simulations of electrostatic microinstabilities have been carried out with the EUTERPE code [30] and validated with dedicated experiments performed during the 2017 experimental campaign in TJ-II [31]. The DR provides information on the density fluctuation wave-number spectra as well as the radial electric field and is used as the basic diagnostic for the characterisation of the plasma edge turbulence. Several ECRH scenarios have been studied in which plasma profiles are modified by changing the heating power and deposition location. Measurements have been compared to numerical simulations in which the plasma profiles and the magnetic configuration used as input are the same as the experimental ones.

Electron-driven modes, which are compatible with trapped electron modes (TEM), were found unstable in the plasma edge region in linear simulations. The range of unstable wave-numbers and the radial location of maximum instability found in simulations are consistent with the relevant wave-numbers and the radial variation of experimental density fluctuations spectra measured by the DR system. Experiments were carried out both with hydrogen and deuterium as base gas, finding no dependency of the power spectra with the bulk ion mass. In agreement with the experiment, simulations with hydrogen and deuterium show very similar results in respect to the radial location of instabilities and unstable wave-numbers, which is consistent with the electron-driven character of the unstable modes found in the simulations. The instabilities are localised toroidally and poloidally in simulations, the location of maximum instability being affected by the rotational transform. A systematic difference is found between the density fluctuation spectra measured by the DR system at poloidally separated positions on the same flux-surface. As in the case of simulations, the poloidal asymmetry of the fluctuation spectra measured by the DR system is also largely affected by the rotational transform. As an example, figure 6 shows in the upper row the perpendicular wavenumber spectra measured at the two poloidally separated plasma regions in the standard and high iota magnetic configurations. An asymmetry is clearly observed in the intensity of the density fluctuations in the whole $k_\perp$ range. In the standard magnetic configuration, higher turbulence level is measured in region 1 as compared with that measured in region 2, see figure 6, left. This asymmetry reverses in the high iota configuration, see figure 6, right. The lower row of figure 6 shows the poloidal localization of instabilities found by the EUTERPE gyrokinetic simulations. Model and experiment agree in showing a poloidal asymmetry that depends on the magnetic configuration. The results are consistent in the high iota configuration. However, there is a strong disagreement in the standard magnetic configuration: the amplitude of the instabilities in the simulations is higher in region 2 than in region 1, opposite to the experimental observations. Future non-linear simulations are foreseen which will allow for a quantitative comparison of fluctuation levels and its spatial dependence. Besides, variations of electric field along the flux-surface could also modify the poloidal variation of fluctuation levels.

3.3. First measurements of density fluctuations in both positive and negative density gradient regions of the plasma

A crucial open issue for next step devices and the fusion reactor is how to achieve particle fuelling in the core plasma in order to replenish the fused nuclei. Pellet fuelling systems designed to inject particles at high speed deep into the plasma are one of the main tools to achieve that goal. However, at reactor relevant plasma densities and temperatures, pellets will hardly be able to reach the core plasma region because pellet ablation will take place in the plasma edge causing plasma bumps with positive and negative density gradient regions [32, 33]. Eventually particles could be transported radially inwards by turbulence. Fluid and gyrokinetic simulations have been used to investigate the level of inward turbulent particle transport in the inverted density gradient region [34, 35] but comparison of simulations with experimental fluctuation levels and fluxes is still missing. First 2D poloidal contour plots of plasma potential and density fluctuations have been measured with the TJ-II HIBP diagnostic [36], which have allowed to characterise turbulence in positive and negative gradient regions: density fluctuations appear both

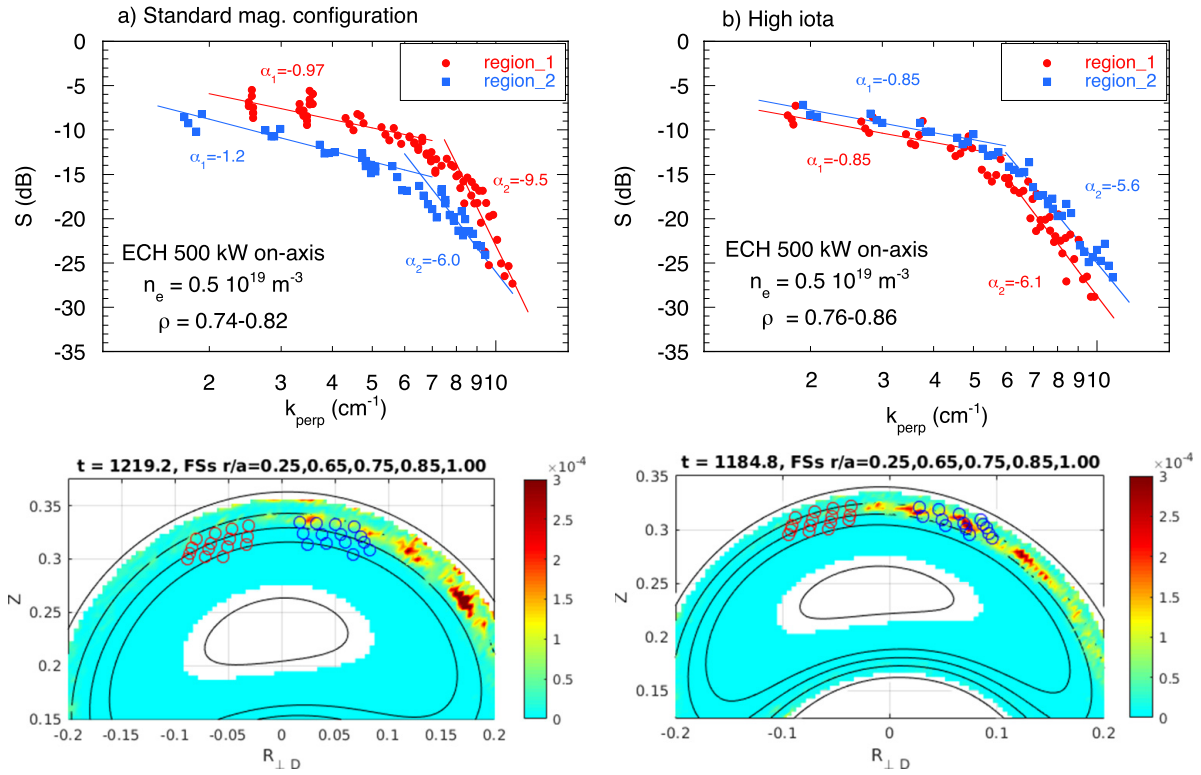

Figure 6. Upper row: experimental $k_\perp$ spectra measured in two plasma regions poloidally separated (see figure 1 caption for the explanation of regions) in the standard (left) and high iota (right) magnetic configurations. Lower row: EUTERPE simulation of the localization of the instabilities for the standard (left) and high iota (right) magnetic configurations. Red and blue circles indicate the left and right DR probing regions, respectively.

at the positive and negative gradient regions, their amplitude being minimum in the zero density gradient zone while it is stronger in the negative than in the positive gradient region [37]. Gyrokinetic simulations performed with EUTERPE for ECRH plasmas yield results consistent with the experiment. In the electron root scenario (positive radial electric field) ion temperature gradient modes are found to be stable due to the nearly flat ion temperature profiles. Linear and collisionless TEM simulations (kinetic ions and electrons) show that the most unstable modes are located in the negative density gradient region [38], in consistency with local measurements of plasma fluctuations quantified by the HIBP diagnostic in ECRH TJ-II scenarios [37].

4. Interplay between radial electric fields, turbulence and atomic physics

A number of research areas related to plasma turbulence in TJ-II, mainly of experimental nature so far, are providing additional valuable results.

4.1. Impact of the edge neutral density fluctuations on the observed turbulent structures

An almost unexplored area of research has been investigated in TJ-II experimentally: the impact of the edge plasma turbulence on the neutrals. The origin of this study is the 2D quantitative measurement of the edge plasma electron density turbulence as obtained using the He I ratio technique with a spectroscopic fast camera system. Comparing the coherent electron density structures (blobs) with those of the raw plasma emission, it is deduced that thermal neutrals react to low frequency plasma fluctuations becoming also turbulent [39]. This result is explained with a simple model that shows how plasma blobs with excess electron density perturb the neutrals density locally through enhanced ionization. This is in agreement with state of the art models that couple consistently plasma turbulence and neutral kinetics [40, 41].

4.2. L–H transition triggered by turbulence stabilization due to both zero and low-frequency varying large scale flows

Mean radial electric fields as well as low frequency ZF-like global oscillations have been identified during the low–high (L–H) transition in hydrogen and deuterium plasmas. No evidence of isotope effect has been observed in the L–H transition dynamics [42]. The intensity of fluctuations in ion current collected by Langmuir probes is significantly suppressed during the L–H transition. However, floating potential fluctuations are compressed to a low frequency range ($f < 10$ kHz) during the L–H transition. These very low frequency fluctuations appear only in potential signals and are the ones that exhibit a global character quantified by the level of long range correlations (LRC) [42]. The different behavior of the frequency spectra of potential and density fluctuations during the L–H transition indicates that LRC are mainly present in potential but not in

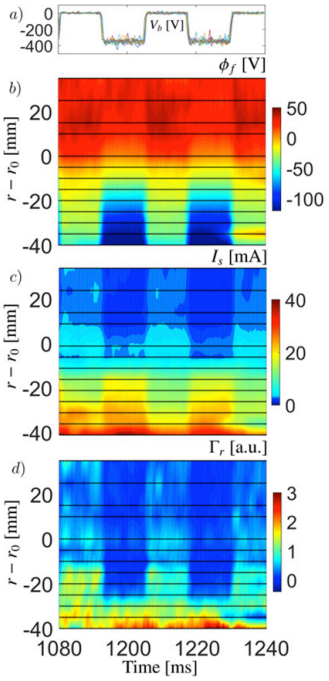

Figure 7. (*a*) Biasing voltage waveform; (*b*)–(*d*) radial profiles of floating potential, ion saturation current and turbulent flux, respectively, during dynamical biasing in the plasma boundary region. $r - r_0 < 0$ corresponds to the plasma edge; $r - r_0 > 0$ corresponds to the SOL.

density fluctuations, which is consistent with the charateristics of low frequency ZF structures. These observations emphasize the critical role of both zero and low frequency varying large-scale flows for stabilising turbulence during the triggering of the L–H transition in magnetically confined toroidal plasmas.

4.3. Impact of the radial electric fields on turbulence spreading in the edge and scrape-off layer

Understanding filamentary and blob transport across the scrape-off-layer (SOL) is a key issue for the design and operation of future devices as it is crucial in determining the power load to the divertor and first wall of the machine. Consequently, clarifying whether the SOL width is set by local effects inside the SOL region or/and by transport arriving from the plasma edge, and the role played by $E_r \times B$ sheared flows in edge-SOL coupling are important issues. The radial transport (spreading) of turbulent energy is a consequence of the redistribution of fluctuation energy from unstable regions with dominant free energy sources to adjacent regions without or with weaker free energy sources.

The spreading of turbulence therefore involves transport from strongly driven (i.e. unstable) to weakly driven regions [43, 44]. Flow shear can 'block' turbulence spreading, decoupling turbulence radially [45, 46]. The influence of radial electric fields on turbulence spreading has been studied experimentally in TJ-II co-NBI heated plasmas ($P_{\mathrm{NBI}} \approx 500$ kW) [47]. A 2D Langmuir probe array [48] was used to measure the floating potential, ion saturation current and turbulence-driven particle transport, neglecting the influence of electron temperature fluctuations. The radial electric field has been modified with the aid of a biasing electrode in the plasma edge, located at $0.85 < \rho < 0.90$ (corresponding to $-48 < r - r_0 < -33$ mm at the Langmuir probe location). The influence of edge biasing on plasma profiles is shown in figure 7. During the negative biasing phase (-300V), the floating potential becomes more negative (figure 7(*b*)) and the perpendicular phase velocity increases [47]. The latter directly reflects changes in radial electric fields induced by edge biasing. Also in this phase, the edge floating potential (figure 7(*b*)) and ion saturation current (figure 7(*c*)) profiles get steeper, while the turbulent particle flux (figure 7(*d*)) is reduced outside the last closed flux surface, concomitant with a reduction of the base level of the ion saturation current. When the $E_r \times B$ sheared flows achieve velocity gradients comparable to the inverse of the turbulence correlation time, they affect the level of turbulence spreading and edge-SOL coupling [47]. Hence, the shearing rate of edge radial electric fields can be an important tool to suppress turbulence and decouple edge and SOL regions.

5. Effect of magnetic configuration on transport

Transport studies in TJ-II, as in many other devices, require the consideration of magnetic configurations where magnetic islands can be present. These are often detected as coherent modes in magnetic signals where, owing to the low poloidal mode numbers of the main low-order rationals of the rotational transform, the helicity can be resolved with the help of a poloidal array of magnetic coils or other diagnostics with some degree of poloidal/toroidal resolution. Since 1D transport codes are well-developed tools for transport analyses, a practical transformation of coordinates has been developed [49] to adapt the metric coefficients of an unperturbed configuration to a new one where the islands (or stochastic) region is excluded. These regions formed by the islands (or stochastic zones) can always be calculated separately if transport is non-trivial in them. This result is illustrated by figure 8. It shows that the analytical model developed in [49] yields values of the metric coefficients for a perturbed magnetic configuration that are in good agreement with the ones obtained numerically from the Poincaré sections. This analytical model, due to its simplicity, constitutes a very practical solution to perform 1D transport in configurations with magnetic islands, where the islands width or location change.

In addition, it is often the case that the magnetohydrodynamic (MHD) modes associated to low order rationals of the rotational transform do not respect the four-fold toroidal periodicity of TJ-II. Theoretical studies on the MHD equilibrium of a four-fold advanced helical device [50] have demonstrated that the energy of periodicity-breaking perturbed configurations exhibit local minima with respect to the perturbation parameter, which lie below the energy of the unperturbed configurations and provide a natural explanation for the ease with which periodicity-breaking MHD modes can be found in real experiments.

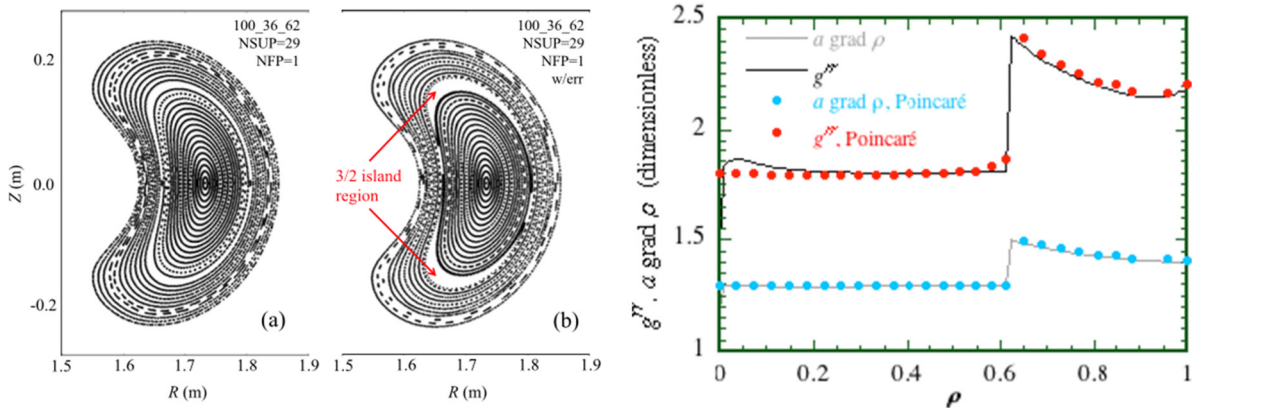

Figure 8. Left: a TJ-II magnetic configuration perturbed by a small error field. Right: comparison between some metric coefficients computed using the analytical annular model with island width 1.7 cm (continuous lines) and numerically obtained from the Poincaré plot with islands in the left part of the figure (dots). Reproduced courtesy of IAEA. Figure from [49]. © EURATOM 2018.

5.1. Investigation of the radial propagation of small, spontaneously generated, temperature perturbations using transfer entropy (TE)

Electron heat transport in fusion plasmas presents significant challenges, among which one may consider extraordinary phenomena such as power degradation, rapid (non-local) transport, and profile stiffness. To study heat transport, we make use of a novel analysis technique, TE, which measures the causal relation or information flow between two time series. This technique has some remarkable properties that converts it into a very sensitive tool to study the propagation of small perturbations in highly non-linear systems, such as fusion plasmas. TE has been firstly validated by analysing the propagation of heat waves in modulated ECRH TJ-II discharges and comparing with traditional Fourier techniques [51].

Then, we have applied it to analyse the propagation of small, spontaneously arising temperature perturbations in non-modulated discharges [52]. We show that heat transport in TJ-II is not a smooth and continuous (diffusive) process, but involves mini-transport barriers associated with low-order rational surfaces and rapid non-local radial 'jumps'. In addition, we find that the non-local contribution to transport becomes more prominent at higher input power. Figure 9 shows the TE between a centrally located electron cyclotron emission (ECE) reference channel and the other available ECE channels. One observes a clear outward propagating 'plume', interrupted by 'trapping zones' (horizontally extended structures) and 'minor barriers' (radial gaps). Interested readers can look at [52] for details. This remarkable finding might shed new light on the nature of anomalous transport.

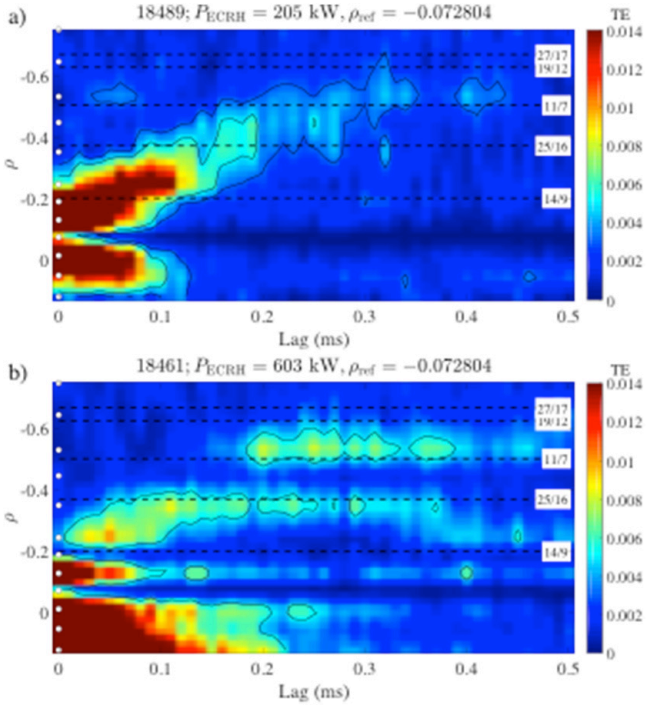

Figure 9. Examples of TE, calculated from ECE data, between a reference channel and the others whose location is indicated by white circles at the left vertical axis. The reference ECE channel is located at $\rho_{ref} \approx -0.07$. Results for two heating powers are shown: (*a*) $P_{ECRH} = 205$ kW and (*b*) $P_{ECRH} = 603$ kW. The color scale indicates the value of *T*. The approximate location of some major rational surfaces is indicated by horizontal dashed lines; the line labels specify the corresponding rotational transform, n/m. Reprinted from [52], with the permission of AIP Publishing.

6. Plasma core fuelling. Pellet physics and modelling

Core fuelling is a critical issue on the pathway to the development of steady-state operational scenarios in magnetic confined plasmas. Cryogenic PI has become a prime candidate for this purpose [53]. A compact pipe-gun type PI has been operated on TJ-II since 2014. Four different pellets can be injected at velocities between 800 and 1200 m s^{-1} into the plasma from its outer edge [54]. In dedicated experiments it was determined that pellet fuelling efficiency (pellet particles deposited in the plasma/number of pellet particles) in TJ-II can range from about ∼20% to ∼80%, this value depending strongly on the pellet penetration depth [27]. Efficiencies tend to be <40% for ECRH plasmas in which pellets do not penetrate beyond the magnetic axis. In contrast, for NBI heated plasmas, in which the core electron temperature is lower

(300–400 eV), the fuelling efficiency is significantly higher. This tendency for increasing efficiency with penetration depth beyond the magnetic axis is considered to be due to inwards effective drifting (towards the magnetic axis) of the partially ionized clouds that surround a pellet (plasmoids) created beyond that point. This has been understood from pellet ablation and deposition simulations made using a TJ-II adapted version of the hydrogen PI 2 code (HPI2) [55] (see figures 19 and 20 therein). Moreover, another study carried on TJ-II has shown that even when pellet particle density peaking is initially observed outside the core, this can be followed by an inward shift (towards the magnetic axis) of the pellet electrons. [26]. Although pellet injections cannot be performed from the inner plasma edge on TJ-II (equivalent to high-field side injections in tokamaks) these studies indicate that a beneficial inwards drifting of pellet plasmoids may be present in this device.

With the expansion of the TJ-II pellet database it has been observed that pellet fuelling efficiency can benefit from the presence of a population of fast electrons in its plasma core [56]. In fact, for ECRH plasmas, it has been determined that when no fast electrons are detected (by hard x-ray emissions or by excess pellet ablation), this efficiency is typically well below 30%. However, when a fast-electron population exists in the core when an injection is made (i.e. inside $\rho = 0.4$), then pellet penetration is truncated and fuelling increase by up to 50% [56]. Simulations of post-injection electron density profiles made with the TJ-II HPI2 code are in good agreement with Thomson scattering density profiles for the former case. However, there are significant discrepancies between the simulated and experimental density profiles for latter case as the current TJ-II version of HPI2 code does not consider fast-electron effects [55]. Although the physics behind this increase is unclear at present, it is considered that pellet vaporization due to an abrupt heating of the ice may lead to a disruption of the processes of neutral cloud and plasmoid expansion and drift that normally occur. Other hypotheses, such as fast electron impacts causing a rocket effect that results in pellet deflection, also need to be investigated. In order to check these hypotheses it will be necessary to obtain fast-frame camera images captured from different viewing positions using a multiple-branch coherent fibre bundle. This will allow comparisons of plasmoid evolution along the magnetic field lines, and subsequent drifting across field lines. Also, modifications need to be made to the TJ-II version of HPI2 code. For instance, implementation of functions that consider excess ablation due to fast electrons or drift velocity modifications for plasmoids born at plasma radii where fast electrons occur could be implemented in order to achieve satisfactory agreement between simulated and experimental profiles.

As discussed in section 2, the need to explore favourable operation scenarios capable of preventing impurity accumulation is critical [57]. One method for performing such studies is the tracer-encapsulated solid-pellet (TESPEL) technique in which a hollow polystyrene shell, $(-\mathrm{CH}(\mathrm{C_6H_5})\mathrm{CH_2}-)_n$, filled with a known quantity of a suitable tracer element, is injected into a plasma [58]. In consequence, the impurity element is deposited directly in the plasma core, thereby eliminating inward diffusion from the physics.

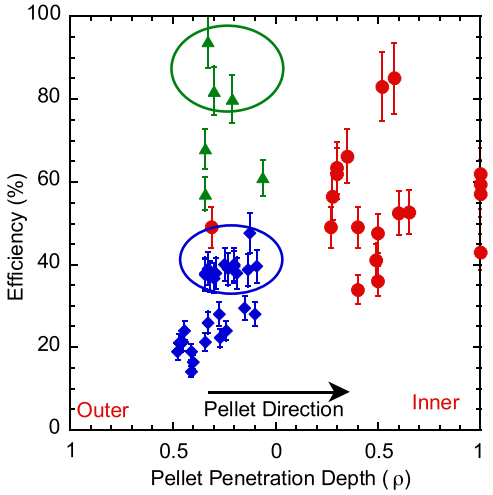

Figure 10. Fuelling/deposition efficiency as a function of pellet penetration depth into TJ-II standard configuration plasmas. The data are for cryogenic hydrogen (filled blue diamonds) and polystyrene (green triangles) pellets injected into ECRH plasmas and cryogenic hydrogen pellets (red dots) injected into NBI plasmas. Cases for which a population of fast electrons is present in the core during PI are contained within the ovals. Examples of pellets that are not fully ablated within the plasma are plotted on the right axis.

Recently, a TESPEL injector was temporarily piggy-backed onto the up-stream end of the TJ-II PI [59, 60], thereby making it a unique system as both pellet types, cryogenic and tracer filled, can be injected along adjoining guide tubes into the same toroidal sector of TJ-II, albeit not simultaneously. Although the *raison d'être* of both PI methods is distinct, both types should undergo the same, or similar, physical processes as they travel through the plasma towards its core. Indeed, for both pellet types, the ablated particles in the plasmoid should experience the same physical effect(s) thus they should undergo similar processes, e.g. drift and diffusion. However, few systematic comparisons of these pellet types exist due to the limited number of devices equipped with both cryogenic and impurity PI systems. Moreover, for reference or comparison purposes, TESPEL pellets with no tracer are sometimes injected in TJ-II [61].

In a comparative study, it was shown that the post-injection electron density increase, after an injection in ECRH plasma, is significantly higher for carbon/hydrogen pellets than for solid hydrogen pellets (having similar electron content), as shown in figure 10. This is due to a reduction in plasmoid outwards drift for the former that is inversely proportional to particle atomic mass [62]. Although it is considered that pellet cloud pressure will be higher for hydrogen pellets, this is not sufficient to offset the higher carbon mass contribution.

Although it was reported in [61] that excess ablation was observed after penetration inside $\rho = 0.4$ for TESPEL pellets with no tracer, it was not appreciated therein that

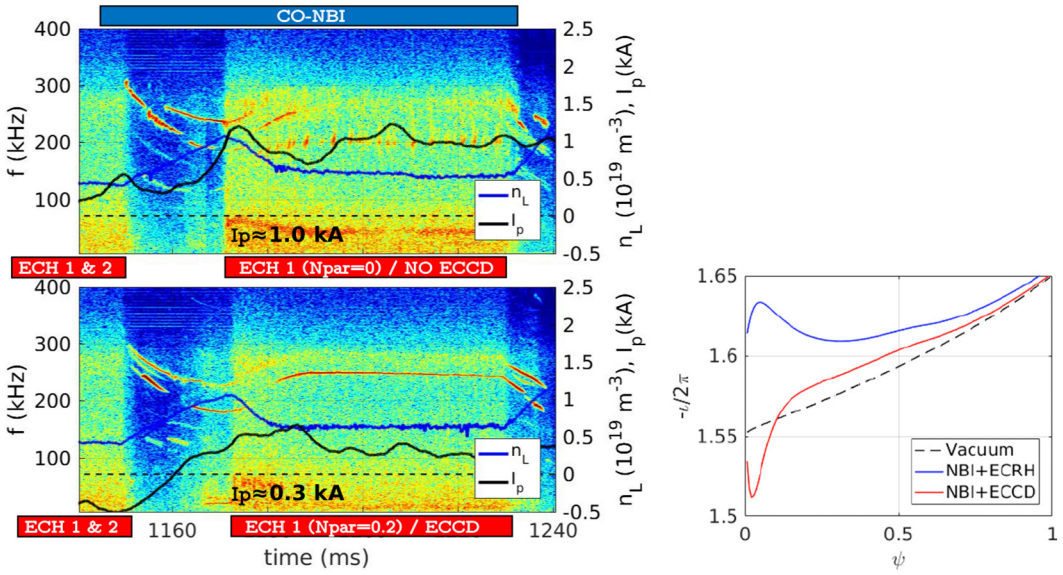

Figure 11. Left: spectrograms of magnetic fluctuations measured with a Mirnov coil for two plasma discharges with (upper box) and without (lower box) on-axis ECCD. Time traces of line average density (blue) and measured plasma current (black) are superimposed on both spectrograms. Right: modelled iota profiles corresponding to the two discharges on the left: blue and red color correspond to the cases without and with ECCD, respectively. The dashed line represents the vacuum iota profile.

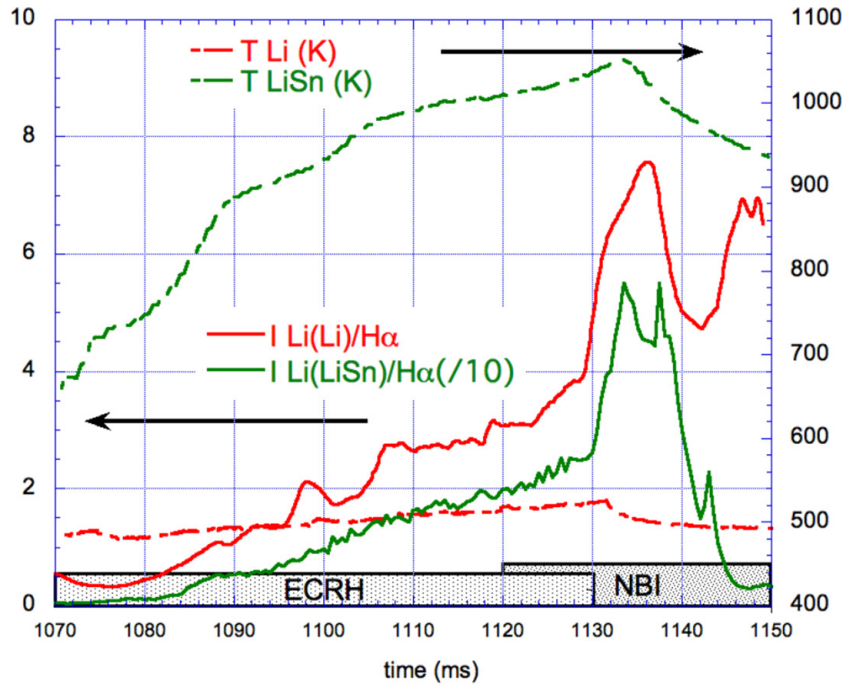

Figure 12. Evolution of Li intensity, normalised to the H_a signal, for pure Li (red) and LiSn (green) samples during TJ-II plasma discharges (left vertical axis). The surface temperature evolution of the samples is also plotted (right vertical axis). Reproduced from [12]. © 2017 Centro de Investigaciones Energeticas Medioambientales y Tecnologicas.

such excess ablation, which is due to fast electrons, leads to an enhancement of deposition efficiency. Simulation of the TESPEL pellet injections using the TJ-II version of the HPI2 code will be complicated as the processes of polystyrene sublimation, carbon ionization, etc need to be considered. Nonetheless, it is intended to continue with TESPEL injections into TJ-II plasmas and record images of the ablation and drift processes with the fast-camera system. It is hoped that this will help shed new light on pellet ablation physics.

7. Control of fast particle driven MHD modes

A number of previous studies have explored the influence of ECH scenarios and magnetic configuration on the alfvénic activity observed in TJ-II, see [63, 64] and references therein. Recent experiments have been carried out in TJ-II NBI plasmas using ECRH on-axis with and without electron cyclotron current drive (ECCD), in order to study the influence of ECCD on the observed Alfvén eigenmodes (AEs) activity [65]. As shown in figure 11, a small amount of negative on-axis ECCD,

just −0.7 kA, is added to the positive NBCD contribution, resulting in a lower total plasma current. This minor change has a strong impact on the observed Alfvénic activity: a steady mode in amplitude and frequency shows up. To understand the changes measured in the AEs spectrum, the influence of the different contributions to the plasma current (NBCD, ECCD, Bootstrap) [66] on the rotational transform profile has been calculated on the basis of the measured plasma profiles. Then, the resulting rotational transform profile is computed and used to obtain the shear Alfvén spectrum (SAS) by means of the STELLGAP code [67]. When EC current is driven, only the plasma current varies. The rest of the parameters of the discharge are barely modified. In particular, density profiles, which are needed for the SAS calculation, show negligible differences. The result indicates that the experimentally observed steady frequency mode could correspond to modes appearing in the $HAE_{2,1}$ gap. This gap becomes wider as the iota profile evolves from the pure NBI to the NBI + ECCD case, thus favouring the presence of the mode in the latter case.

8. Alternative plasma facing components based on liquid metals

Two liquid metals (LM), Li and LiSn, presently considered as alternative materials for the divertor target of a fusion reactor, have been exposed to the plasma in a capillary porous system (CPS) arrangement in TJ-II [68]. A negligible perturbation of the plasma has been recorded in both cases, even when stellarator plasmas are particularly sensitive to high Z elements due to the tendency to central impurity accumulation.

The surface temperature of the LM CPS samples (made of a tungsten mesh impregnated in LiSn or Li) has been measured during the plasma pulse with ms resolution by pyrometry and the thermal balance during heating and cooling has been used to obtain the thermal parameters of the LiSn and Li CPS arrangements, as can be seen in figure 12. Temperatures as high as 1150 K during TJ-II plasma exposure were observed for the LiSn solid case. The melting point of the LiSn alloy is 310 °C. According to the pyrometer reading, surface temperatures of the LiSn finger were above this value during plasma exposure, even in those cases in which it was initially exposed as a solid. However, in some instances visual inspection showed that only partial melting had occurred. Strong changes in the thermal conductivity of the alloy were recorded in the cooling phase at temperatures close to the nominal melting point. The deduced values for the thermal conductivity of the LiSn alloy/CPS sample were significantly lower than those predicted from their individual components. However, a bad thermal contact between the alloy and the supporting mesh due to incomplete wetting, cannot be ruled out at this stage. This would lead to an overheating of the surface while the material in direct contact with the mesh could have remained below the melting point.

With respect to the potential use of LiSn alloys as LM for an alternative target in DEMO, the results obtained in TJ-II agree with the expectations from laboratory results, namely a dominant Li emission from the alloy when exposed to the plasma, in spite of its minority in its composition. A search for characteristic Sn I and Sn II lines in the visible, as well as Sn III and Sn IV lines in the VUV (50–80 nm), did not yield evidence of the presence of tin in the plasma even for the most potentially perturbing conditions. Together with the very low H retention reported previously [69], the use of this alloy can be considered in a reactor. However, it must be pointed out that, in comparison with Li and Sn, the information about this alternative LM alloy is rather scarce. In particular, the low thermal conductivity inferred from the T versus t data and the possible depletion of Li from the alloy at long exposure times remain as potential showstoppers at present. More experimental work is required to fully validate this promising option.

9. Summary

The TJ-II team exploits the outstanding configuration flexibility of the device and its set of advanced diagnostics to provide experimental results in some key fusion research areas.

Reinforced capability in theory and modelling is allowing comparison and validation activities (neoclassics, gyrokinetics, pellet fuelling) and the study of optimized magnetic configurations.

TJ-II research is primarily focused on supporting the stellarator line development (W7-X, LHD) as well as contributing to ITER and ITPA research plans. Substantial resources are being invested as well, with EUROfusion support, in manning and data analysis of W7-X diagnostics and in theory and modelling collaborative activities.

Acknowledgments

This work has been carried out within the framework of the EUROfusion Consortium and has received funding from the Euratom research and training programme 2014–2018 under Grant Agreement No. 633053. The views and opinions expressed herein do not necessarily reflect those of the European Commission. It has been partially funded by the Ministerio de Ciencia, Inovación y Universidades of Spain under projects ENE2013-48109-P, ENE2015-70142-P and FIS2017-88892-P. It has also received funds from the Spanish Government via mobility grant PRX17/00425. The authors thankfully acknowledge the computer resources at MareNostrum and the technical support provided by the Barcelona S.C. It has been supported as well by The Science and Technology Center in Ukraine (STCU), Project P-507F.

ORCID iDs

E. Ascasíbar https://orcid.org/0000-0001-8124-0994
D. Alegre https://orcid.org/0000-0002-1665-7811
A. Alonso https://orcid.org/0000-0001-6863-8578
A. Baciero https://orcid.org/0000-0003-1717-3509
J.M. Barcala https://orcid.org/0000-0002-1092-7091
I. Calvo https://orcid.org/0000-0003-3118-3463
A. Cappa https://orcid.org/0000-0002-2250-9209
B. Carreras https://orcid.org/0000-0001-7921-4690

A. de Castro https://orcid.org/0000-0003-2620-9825
A.W. Cooper https://orcid.org/0000-0003-1989-1926
A. Dinklage https://orcid.org/0000-0002-5815-8463
L. Eliseev https://orcid.org/0000-0002-2787-2103
T. Estrada https://orcid.org/0000-0001-6205-2656
J.M. Fontdecaba https://orcid.org/0000-0001-7678-0240
I. García-Cortés https://orcid.org/0000-0002-5223-391X
J.M. García-Regaña https://orcid.org/0000-0001-7632-3357
C. Hidalgo https://orcid.org/0000-0002-0736-7855
P. Khabanov https://orcid.org/0000-0002-6004-2005
E. de la Luna https://orcid.org/0000-0002-5420-0126
K.J. McCarthy https://orcid.org/0000-0002-5881-1442
B. van Milligen https://orcid.org/0000-0001-5344-6274
B. Momo https://orcid.org/0000-0001-7760-8960
M. Ochando https://orcid.org/0000-0001-7521-4503
S. Ohshima https://orcid.org/0000-0003-1341-4969
J.L. de Pablos https://orcid.org/0000-0002-3850-0196
F. Parra https://orcid.org/0000-0001-9621-7404
I. Pastor https://orcid.org/0000-0003-0891-0941
E. Sánchez https://orcid.org/0000-0003-1062-7870
E.R. Solano https://orcid.org/0000-0002-4815-3407
F.L. Tabarés https://orcid.org/0000-0001-7045-8672
D. Tafalla https://orcid.org/0000-0001-5669-1419
J.L. Velasco https://orcid.org/0000-0001-8510-1422

References

[1] McCormick K. *et al* 2002 *Phys. Rev. Lett.* **89** 015001
[2] Ida K. *et al* 2009 *Phys. Plasmas* **16** 056111
[3] García-Regaña J.M. *et al* 2013 *Plasma Phys. Control. Fusion* **55** 074008
[4] García-Regaña J.M. *et al* 2017 *Nucl. Fusion* **57** 056004
[5] Velasco J.L. *et al* 2018 *Plasma Phys. Control. Fusion* **60** 074004
[6] Calvo I. *et al* 2018 *Nucl. Fusion* **58** 124005
[7] García-Regaña J.M. *et al* 2018 *Plasma Phys. Control. Fusion* **60** 104002
[8] Mollén A. *et al* 2018 *Plasma Phys. Control. Fusion* **60** 084001
[9] Calvo I. *et al* 2017 *Plasma Phys. Control. Fusion* **59** 055014
[10] Calvo I. *et al* 2018 *J. Plasma Phys.* **84** 905840407
[11] Dinklage A. *et al* 2013 *Nucl. Fusion* **53** 063022
[12] Velasco J.L. *et al* 2017 *Nucl. Fusion* **57** 016016
[13] Takeiri Y. *et al* 2017 *Nucl. Fusion* **57** 102023
[14] Helander P. *et al* 2017 *Phys. Rev. Lett.* **118** 155002
[15] Pedrosa M.A. *et al* 2015 *Nucl. Fusion* **55** 052001
[16] Klinger T. *et al* 2017 *Plasma Phys. Control. Fusion* **59** 014018
[17] Wolf R.C. *et al* 2017 *Nucl. Fusion* **57** 102020
[18] Pablant N.A. *et al* 2018 *Phys. Plasmas* **25** 022508
[19] Sánchez E. *et al* 2013 *Plasma Phys. Control. Fusion* **55** 014015
[20] Helander P. *et al* 2011 *Plasma Phys. Control. Fusion* **53** 054006
[21] Mishchenko A., Helander P. and Könies A. 2008 *Phys. Plasmas* **15** 72309
[22] Monreal P. *et al* 2016 *Plasma Phys. Control. Fusion* **58** 045018
[23] Monreal P. *et al* 2017 *Plasma Phys. Control. Fusion* **59** 065005
[24] Jenko F. *et al* 2000 *Phys. Plasmas* **7** 1904
[25] Jost G. *et al* 2001 *Phys. Plasmas* **8** 3321
[26] Velasco J.L. *et al* 2016 *Plasma Phys. Control. Fusion* **58** 084004
[27] McCarthy K.J. *et al* 2017 *Nucl. Fusion* **57** 056039
[28] Alonso J.A. *et al* 2017 *Phys. Rev. Lett.* **118** 185002
[29] Sánchez E. *et al* 2018 *Plasma Phys. Control. Fusion* **60** 094003
[30] Sánchez E. *et al* 2019 *Nucl. Fusion* **59** 076029
[31] Estrada T. *et al* 2019 *Nucl. Fusion* **59** 076021
[32] Valovic M. *et al* 2008 *Nucl. Fusion* **48** 075006
[33] Vincenzi P. *et al* 2015 *Nucl. Fusion* **55** 113028
[34] Garzotti L. *et al* 2014 *Plasma Phys. Control. Fusion* **56** 035004
[35] Angioni C. *et al* 2017 *Nucl. Fusion* **57** 116053
[36] Sharma R. *et al* 2018 Poloidal 2D scans to investigate potential and density profiles in the TJ-II stellarator using heavy ion beam probe *45th EPS Conf. on Plasma Physics (Prague, Czech Republic, 2–6 July 2018)* vol 42A p P5.1061 (https://eps2018.eli-beams.eu/en)
[37] Sharma R. *et al* unpublished
[38] Sánchez E. *et al* unpublished
[39] de la Cal E. 2016 *Nucl. Fusion* **56** 106031
[40] Wersal C. and Ricci P. 2015 *Nucl. Fusion* **55** 12304
[41] Thrysøe A.S. *et al* 2018 *Nucl. Fusion* **58** 096005
[42] Losada U. *et al* 2018 *Plasma Phys. Control. Fusion* **60** 074002
[43] Garbet X. *et al* 1994 *Nucl. Fusion* **34** 963
[44] Mattor N. *et al* 1994 *Phys. Rev. Lett.* **72** 486
[45] Wang W.X. *et al* 2007 *Phys. Plasmas* **14** 072306
[46] Beyer P. *et al* 2000 *Phys. Rev. Lett.* **85** 4892
[47] Grenfell G. *et al* 2019 *Nucl. Fusion* **59** 016018
[48] Alonso A. *et al* 2012 *Nucl. Fusion* **52** 063010
[49] López-Bruna D. *et al* 2018 *Nucl. Fusion* **58** 106031
[50] Cooper A.W. *et al* 2018 *Nucl. Fusion* **58** 124002
[51] van Milligen B.Ph. *et al* 2017 *Nucl. Fusion* **57** 056028
[52] van Milligen B. *et al* 2018 *Phys. Plasmas* **25** 062503
[53] Combs S.K. and Baylor L.R. 2018 *Fusion Sci. Technol.* **73** 493
[54] Combs S.K. *et al* 2013 *Fusion Sci. Technol.* **64** 513
[55] Panadero N. *et al* 2018 *Nucl. Fusion* **58** 026025
[56] McCarthy K.J. *et al* 2019 *Plasma Phys. Control. Fusion* **61** 014013
[57] Burhenn R. *et al* 2009 *Nucl. Fusion* **49** 065005
[58] Sudo S. *et al* 2012 *Rev. Sci. Instrum.* **83** 023503
[59] Tamura N. *et al* 2016 *Rev. Sci. Instrum.* **87** 11D619
[60] McCarthy K.J. *et al* 2018 *Phys. Scr.* **93** 035601
[61] McCarthy K.J. *et al* 2017 *Europhys. Lett.* **120** 25001
[62] Matsuyama A. *et al* 2012 *Plasma Fusion Res. Lett.* **7** 1303006
[63] Nagaoka K. *et al* 2013 *Nucl. Fusion* **53** 072004
[64] Melnikov A.V. *et al* 2016 *Nucl. Fusion* **56** 076001
[65] Cappa A. *et al* 2018 Impact of ECCD on Alfvén eigenmodes in the TJ-II stellarator *45th EPS Conf. on Plasma Physics (Prague, Czech Republic, 2–6 July 2018)* vol 42A p P4.1040 (https://eps2018.eli-beams.eu/en)
[66] Velasco J.L. *et al* 2011 *Plasma Phys. Control. Fusion* **53** 115014
[67] Spong D., Sánchez R. and Weller A. 2003 *Phys. Plasmas* **10** 3217
[68] Tabarés F.L. *et al* 2017 *Phys. Scr.* **T170** 014054
[69] Tabarés F.L. *et al* 2016 *Nucl. Mater. Energy* **12** 1368